Proceedings of the Thirty-fourth (2024) International Ocean and Polar Engineering Conference **www.isope.org**
Rhodes, Greece, June 16–21, 2024

ISBN 978-1-880653-78-4; ISSN 1098-6189

A Comparative Study between Wall-Resolved and Wall-Modeled Large Eddy Simulation of Turbulent Channel Flows

Guoqing Fan[1], Jie Zhu[2], Weiwen Zhao[1], Decheng Wan[1]*

[1] Computational Marine Hydrodynamics Lab (CMHL), School of Naval Architecture, Ocean and Civil Engineering, Shanghai Jiao Tong University, Shanghai, China
[2] Wuhan Second Ship Design and Research Institute, Wuhan, China

[*]Corresponding Author

ABSTRACT

In this paper, turbulent channel flow at $Re_\tau \approx 1000$ is numerically simulated using both wall-resolved large eddy simulation (WRLES) and wall-modeled large eddy simulation (WMLES) methods. In addition to comparing the near-wall velocity distribution and Reynolds stresses, we specifically focused on the predictive accuracy of the two methods for wall pressure fluctuation. The two-dimensional (consisting of wavenumber and frequency) spectra are analyzed and compared with data from direct numerical simulation (DNS). The results demonstrate the predictive accuracy of both methods in terms of time-averaged quantities. Regarding wall pressure fluctuation, both methods effectively capture the convective ridge where energy is concentrated. However, due to modeling of the inner layer of the boundary layer, the WMLES inevitably incurs predictive errors in spectra level.

KEY WORDS: Wall-resolved large eddy simulation (WRLES); wall-modeled large eddy simulation (WMLES); wall pressure fluctuations; wavenumber-frequency spectra.

INTRODUCTION

Wall pressure fluctuations are the primary source of flow-generated noise in turbulent wall-bounded flows. Enhancing the accuracy and efficiency of numerical simulations regarding this phenomenon holds great significance for addressing most engineering concerns. Currently, numerical simulations of wall pressure fluctuations primarily involve direct numerical simulation (DNS), wall-resolved large eddy simulation (WRLES), hybrid LES/RANS methods, and wall-modeled large eddy simulation (WMLES). DNS, as a highly accurate simulation approach, directly solves the Navier-Stokes equations on a very fine grid. Because it captures every detail in the unsteady flow fields, this renders computational cost quite substantial and it is primarily suitable for low Reynolds number basic flows. LES, as an alternative approach to DNS, focuses on resolving the large-scale structures in the flow field. For the unresolved part of the scale, LES employs subgrid-scale (SGS) models. Due to its higher computational accuracy compared to Reynolds-Averaged Navier-Stokes (RANS) in predicting flow fluctuations, vortex structures, and flow-induced noise, LES has broader prospects for applications in the engineering field.

In the academic research field, LES has become an indispensable engineering tool for predicting and analyzing unsteady, multiscale, and Multiphysics turbulent flows. In practical engineering applications, LES is not widely utilized, mainly due to the high computational demands of WRLES for high Reynolds number flows (Piomelli and Balaras, 2002). The majority of the computational grid is dedicated to resolving the inner layer of the boundary layer flow (which occupies approximately 10% to 20% of the boundary layer thickness). As a consequence, the fundamental idea of WMLES is to directly compute and resolve the flow in the outer layer of the boundary layer, while using modeling approaches for the flow in the inner layer of the boundary layer. Choi and Moin (2012) estimated the computational cost for high Reynolds number boundary layer flows. The study showed that the number of grid nodes of turbulent boundary layers required for DNS, WRLES, and WMLES is proportional to $N_{DNS} \sim Re_L^{37/14}$, $N_{WR} \sim Re_L^{13/7}$, $N_{WM} \sim Re_L$, where L represents the length of the flat plate. Importantly, the computational cost of WMLES exhibits a linear relationship with Reynolds number, which significantly expands the range of Reynolds numbers that WMLES can handle.

Currently, many scholars (Chen et al., 2023; Fan et al., 2024; He et al., 2024) have numerically simulated various flow phenomena at different Reynold numbers using WMLES. For channel flow with zero adverse pressure gradient, Mukha et al. (2019) conducted numerical simulations using an algebraic wall stress model based on laws of the wall, successfully predicting the mean velocity profile of fully developed turbulent channel flow at $Re_\tau \approx 5200$. Zhao et al. (2023) conducted numerical simulations of channel flow at $Re_\tau \approx 1000$ using the equilibrium wall stress model and studied the effects of different SGS models in combination with WMLES. Suga et al. (2019) employed the non-equilibrium wall stress model and considered all the terms of thin boundary layer equation (TBLE) to numerically simulated turbulent channel flow at $Re_\tau \approx$ 1000-5000. Wang et al. (2020) focused on the spectral energy distribution predicted by WMLES in the outer region of

wall-bounded turbulent flows at moderately high Reynolds numbers up to $Re_\tau \approx 5200$. Park and Moin (2016) employed WMLES to numerically simulate channel flow at $Re_\tau \approx 2000$, with a focus on the accuracy of WMLES in predicting wall pressure fluctuations. The results showed that the grid resolution requirements for predicting wall pressure fluctuations are more stringent than those for velocity predictions. Under the condition of $\delta/\Delta x > 20$ and $\delta/\Delta z > 30$, the low-frequency component of the pressure fluctuation spectrum matched well with DNS and experimental data.

Previous research on WMLES has predominantly focused on time-averaged quantities or statistical quantities, with relatively less evaluation of WMLES in terms of fluctuating quantities. In present study, we conduct numerical simulations of channel flow at $Re_\tau \approx 1000$ using the open-source computational fluid dynamics platform OpenFOAM, employing both WRLES and WMLES methods. In addition to comparing the near-wall velocity distribution and Reynolds stresses, we place special emphasis on the predictive accuracy of wall pressure fluctuation. The one-dimensional spectra and two-dimensional wavenumber-frequency spectra of wall pressure fluctuation are analyzed and compared with DNS data (Yang and Yang, 2022).

NUMERICAL METHODOLOGY

Governing Equations

LES is incapable of resolving vortices of all scales in the flow field. By applying a filter to the incompressible N-S equations (Sagaut, 2005), the governing equations for LES can be obtained.

$$\frac{\partial \tilde{u}_i}{\partial x_i} = 0 , \tag{1}$$

$$\frac{\partial \tilde{u}_i}{\partial t} + \frac{\partial \tilde{u}_i \tilde{u}_j}{\partial x_j} = -\frac{1}{\rho}\frac{\partial \tilde{p}}{\partial x_i} + \nu \frac{\partial^2 \tilde{u}_i}{\partial x_j \partial x_j} + \frac{\partial \tau_{ij}^{sgs}}{\partial x_j} , \tag{2}$$

where $\tilde{u}_i$ (i = 1, 2, 3) is the filtered velocity component in the x_i direction of the flow field, $\tilde{p}$ is the filtered pressure of the flow field, ν is the kinematic viscosity of the fluid and τ_{ij}^{sgs} is the SGS stress term. τ_{ij}^{sgs} is given by

$$\tau_{ij}^{sgs} = 2\nu_{sgs}\tilde{S}_{ij} + \frac{1}{3}\tau_{kk}^{sgs}\delta_{ij} , \tag{3}$$

where $\tilde{S}_{ij}$ is the resolved strain-rate tensor, δ_{ij} is the Kronecker delta, ν_{sgs} is the SGS eddy viscosity. In this study, the wall-adapting local eddy-viscosity (WALE) model (Nicoud and Ducros, 1999) is applied as

$$\nu_{sgs} = (C_w \Delta)^2 \frac{(S_{ij}^d S_{ij}^d)^{3/2}}{(\tilde{S}_{ij}\tilde{S}_{ij})^{5/2} + (S_{ij}^d S_{ij}^d)^{5/4}} , \tag{4}$$

where $C_w = 0.325$ is the WALE coefficient, Δ is the cube root of local cell volume, S_{ij}^d is the traceless symmetric part of the square of the velocity gradient tensor.

Wall stress modeling

For equilibrium wall stress model (EQWM), the starting point is the simplified TBLE (Wang and Moin, 2002). In the inner layer of the boundary layer, the pressure gradient in the wall-normal direction is assumed to be zero. As a result, the N-S equations within the boundary layer can be simplified as

$$\frac{\partial}{\partial x_2}\left[(\nu + \nu_t)\frac{\partial u_i}{\partial x_2}\right] = F_i , \quad i = 1,3 , \tag{5}$$

where F_i is source term,

$$F_i = \frac{1}{\rho}\frac{\partial p}{\partial x_i} + \frac{\partial u_i}{\partial t} + \frac{\partial}{\partial x_j}u_i u_j . \tag{6}$$

The turbulent eddy viscosity is obtained from the mixing length theory (Van Driest, 1956) with a near-wall damping function

$$\nu_t = \kappa \nu x_2^+ (1 - e^{-x_2^+/A})^2 , \tag{7}$$

where A = 17.8. The wall stress model sample F_i from the LES domain, resulting in a constant source term. Eq. 5 then degenerates into an ordinary differential equation. The EQWM sets the source terms F_i to zero. By integrating Equation Eq. 5 from the wall to the sampling point, the boundary condition for wall shear stress can be obtained.

$$\tau_{wi} = \mu \left.\frac{\partial u_i}{\partial x_2}\right|_{x_2=0} = \frac{\rho u_{h_i}}{\int_0^h \frac{dx_2}{\nu + \nu_t}} , \tag{8}$$

where i = 1, 3. μ represents the dynamic viscosity of the fluid, h is the sampling height, and u_{h_i} is the velocity at the sampling point in the LES domain. The EQWM only requires sampling the streamwise and spanwise velocity components at the sampling point. The correct $\tau_w = (\tau_{w1}^2 + \tau_{w3}^2)^{1/2}$ is evaluated using the instantaneous τ_{wi} values from the previous time step and then enforced as a boundary condition, by setting a turbulent viscosity ν_t at the wall

$$\nu_t = \frac{\tau_w}{\rho \left.\frac{\partial u_i}{\partial x_2}\right|_{x_2=0}} - \nu , \tag{9}$$

NUMERICAL SETUP

Computational domain and mesh

The computational domain and mesh are described below. Fig. 1 shows the computational domain in all cases and the size is set to $L_x \times L_y \times L_z = 2\pi\delta \times 2\delta \times \pi\delta$, where δ = 1m is the channel half-height, x, y and z denote the streamwise, wall-normal and spanwise directions, respectively. As for the boundary conditions, periodic boundary conditions are applied in the streamwise and spanwise directions, while a no-slip velocity boundary condition and a zero-gradient pressure condition are prescribed at the top wall and bottom wall. A source term is introduced into the momentum equation to maintain the bulk mean velocity U_b to a constant. The Reynolds numbers based on the bulk velocity and friction velocity are $Re_b = U_b\delta/\nu = 20000$ and $Re_\tau = u_\tau\delta/\nu = 1000$, where $u_\tau = \sqrt{\tau_w/\rho}$ is the friction velocity on the wall.

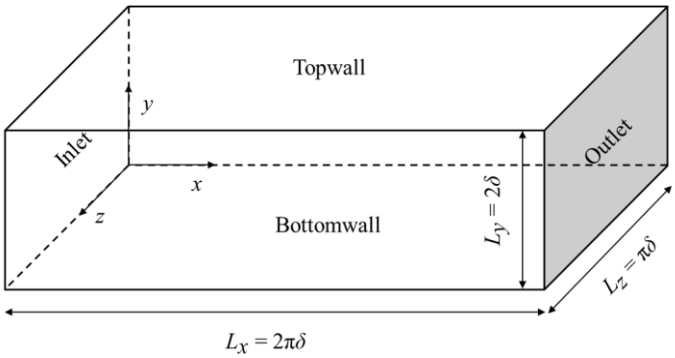

Fig. 1 Computational domain

Fig. 2 (a) and (b) show the computational meshes for WRLES and WMLES, respectively. The key parameters of meshes are demonstrated in Table 1, where $N_x \times N_y \times N_z$ are the numbers of grid points in three directions, N_{total} is the total number of grid points, Δx^+, Δy^+ and Δz^+ are the non-dimensional grid spacings, Δt^+ is the non-dimensional computational time step. In this paper, variables with superscript '+' are non-dimensionalized using characteristic length ν/u_τ and characteristic velocity u_τ. For WRLES, the non-dimensional cell sizes in the wall-normal direction grow gradually from 0.79 at the wall to 15.0 using a linear stretching ratio of 1.05, after which it is uniform. For WMLES, the mesh resolutions in three directions are $\delta/\Delta x = 20$, $\delta/\Delta y = 50$ and $\delta/\Delta z = 40$, respectively. In terms of sampling height, Mukha et al. (2019) compared the predicted errors in channel flow when using flow field information from different grid centers in the wall-normal direction as input values for the wall model. The study pointed out that sampling positions should be avoided at the first grid center off the wall. In addition, some studies (Larsson et al., 2016; Yang et al., 2017) have suggested that setting the sampling height at the first cell off the wall may lead to a log-layer mismatch (LLM). In present study, the sampling height is set at the third grid center, $h = 3^{rd}$ and the distance of the sampling point from the wall is $\Delta h_{wm} = 5\%\delta$ ($\Delta h_{wm}^+ = 50$).

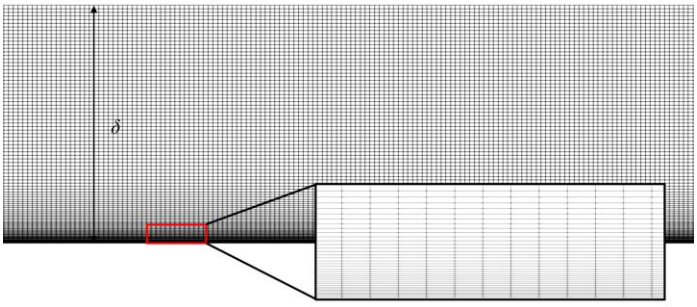

(a) WRLES

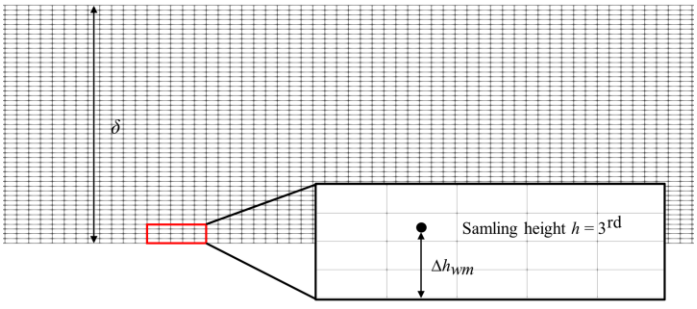

(b) WMLES

Fig. 2 Computational meshes

Table 1. Parameters of computational meshes

Case	WRLES	WMLES
$N_x \times N_y \times N_z$	315 × 217 × 315	127 × 101 × 127
Δx^+	20.0	49.8
Δy^+	0.79 ~ 15.0	20.0
Δz^+	10.0	24.9
Δt^+	0.1	0.2
N_{total}	21.5 million	1.6 million

Numerical schemes and solver

In terms of the numerical schemes and solver, the coupled pressure-velocity is solved using the PISO algorithm (Issa, 1986), with four pressure corrections at each time step. In addition, the temporal term employs the second-order implicit backward scheme (Jasak, 1996). The gradient and Laplacian terms are discretized using the second-order linear scheme. Regarding the discretization of the convective term, WRLES and WMLES employ different numerical discretization schemes. For WRLES, the second-order central differencing is used for the convection term in the N-S equations. However, for WMLES, given the relatively coarse grid near the wall, employing the common linear interpolation scheme used in WRLES could potentially introduce numerical oscillations. The use of the upwind scheme will introduce additional numerical dissipation, but it provides relatively better computational stability. In present study, numerical simulation for WMLES adopt the linear upwind stabilized transport (LUST) scheme (Martínez et al., 2015; Weller, 2012). This scheme uses a weighted average of 75% linear central and 25% linear upwind scheme to compute cell-face values, resulting in second-order accuracy.

RESULTS AND DISCUSSIONS

In this section, we conduct numerical simulations of channel flow at $Re_\tau \approx 1000$ employing both WRLES and WMLES methods. Simulations are run for 18 flow-past times for flow development and statistical time span covers 20 flow-past times. We first compare the predictive accuracy of the two methods on time-averaged quantities. Furthermore, we specifically focus on the predictive accuracy of both methods for wall pressure fluctuation. The one-dimensional spectra and two-dimensional wavenumber-frequency spectra of wall pressure fluctuation are analyzed and compared with DNS data.

Velocity profiles and Reynolds stresses

Fig. 3 shows the mean streamwise velocity profile. The results of WRLES match well with empirical formulas in both the viscous sublayer and logarithmic layer. While WMLES does not resolve the viscous sublayer, its results in the logarithmic layer also align well with empirical formulas. The use of the wall model largely resolves the mismatch issue with the logarithmic law that arises when the near-wall grid is relatively coarse. In addition, the wall friction velocities u_τ predicted by WRLES and WMLES are 9.90×10^{-3} and 9.93×10^{-3}, respectively, showing good agreement with the theoretical value of 1×10^{-2}.

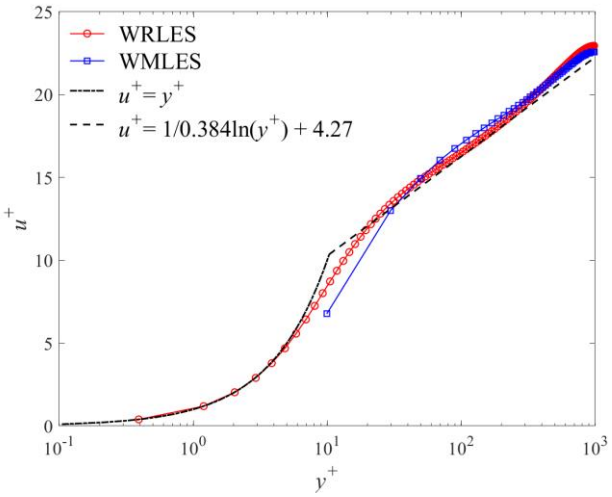

Fig. 3 Streamwise mean velocity profiles

Fig. 4 shows the resolved Reynolds stresses (the velocity component variances and covariance) in inner scaling, which are compared with the DNS data (Yang and Yang, 2022). For the Reynolds stress components $\langle vv\rangle^+$, $\langle ww\rangle^+$ and $\langle uv\rangle^+$, the agreement between the DNS data and the two methods is satisfactory. However, for the $\langle uu\rangle^+$ component, WRLES results match well with DNS data in the inner layer but show relatively underprediction in the outer layer. The overall accuracy of Reynolds stress is lower than that of the mean velocity profiles, which is expected as second-order statistics are generally more challenging to accurately capture. In the case of WMLES, the predicted error of $\langle uu\rangle^+$ shows significant differences from DNS, with an overprediction in the near-wall region and an underprediction in the channel center. This behavior is similar to other numerical simulation results and represents a typical error in performing LES on coarse grids. The main reason might be that WMLES does not effectively resolve the velocity fluctuations sources located in the buffer layer.

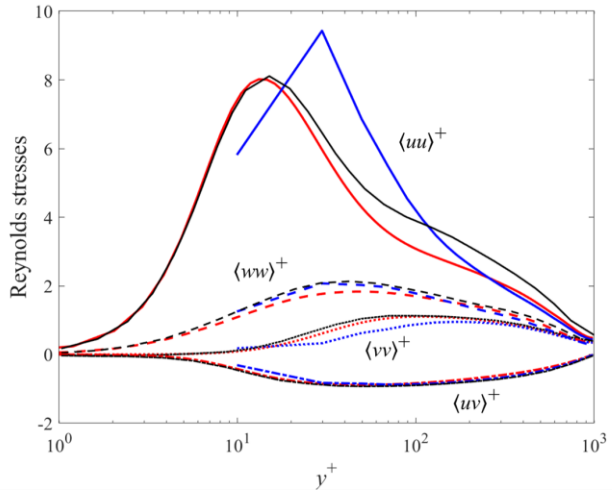

Fig. 4 Inner-scaled Reynolds stresses from WRLES and WMLES. (The red line represents the results of WRLES, the blue line represents the results of WMLES, and the black line shows the DNS data.)

Energy spectra of wall pressure fluctuations

In order to investigate the wavenumber-frequency spectra of wall pressure fluctuations, it is common to place a series of equidistant virtual sensor points along the streamwise or spanwise direction to obtain the spatiotemporal signal of fluctuating pressure. Then the fluctuating pressure data are stored in a two-dimensional matrix: $p(x = m\Delta X, t = n\Delta T)$, where $m = 1, 2, 3, \ldots M$, $n = 1, 2, 3, \ldots N$. ΔX is the spatial interval between sensors, and ΔT represents the sampling interval. In this study, the pressure monitoring point is placed in each grid cell on the wall to solve for higher wavenumbers. Similarly, using a longer array of pressure sensors increases the wavenumber resolution to resolve lower wavenumbers. The sampling interval for all numerical simulations is set to $\Delta T^+ = 0.2$, with a total of 31,400 sampling time steps. The time series is divided into 39 segments with a 50% overlap. Spatial data is not segmented. Spectral leakage is suppressed by multiplying each segment of the time series by a Hanning window. Subsequently, discrete spatiotemporal signals of turbulent fluctuating pressure are subjected to a two-dimensional discrete Fourier transform to obtain Fourier modes as:

$$\hat{p}(k_x,\omega) = \frac{\sqrt{8/3}}{MN}\sum_{m=1}^{M}\sum_{n=1}^{N} w(n\Delta T)\, p(m\Delta X, n\Delta T)\times e^{-i(m\Delta X k_x - n\Delta T\omega)}, \qquad (10)$$

where the coefficient $\sqrt{8/3}$ is included to keep the root mean square of p unchanged after applying the window function $w(t)$. The DC or zero frequency component is removed from all the data in the segment. Ensemble averaging of the squared amplitude yields the wavenumber-frequency spectrum of turbulent fluctuating pressure.

$$\phi_{pp}(k_x,\omega) = \frac{\overline{\hat{p}(k_x,\omega)\,\hat{p}^*(k_x,\omega)}}{\Delta k_x \Delta\omega}, \qquad (11)$$

where $\Delta k_x = 2\pi/M$ is the streamwise wavenumber resolution, $\Delta\omega = 2\pi/N$ is the frequency resolution. Up to this point, the fluctuating pressure is transformed from the space-time domain to the wavenumber-frequency domain.

Fig. 5 compares the one-dimensional spectra of wall pressure fluctuations obtained from WRLES and WMLES calculations, including streamwise wavenumber spectrum, spanwise wavenumber spectrum, and frequency spectrum. All the one-dimensional spectra are integrated from the two-dimensional wavenumber-frequency spectra. For example, integrating the wavenumber along the wavenumber-frequency spectrum yields a one-dimensional frequency spectrum, while the streamwise and spanwise wavenumber spectra are obtained by integrating the corresponding wavenumber-frequency spectra. The spectra are non-dimensionalized using u_τ, τ_w and ν and compared with DNS data (Yang and Yang, 2022). From Fig. 5(a) and Fig. 5(b), it can be observed that for both WRLES and WMLES, as the streamwise wavenumber k_x and frequency ω increase, the amplitude of the one-dimensional spectra initially increases and then decreases. Meanwhile, the amplitude of the one-dimensional spanwise wavenumber spectrum monotonically decreases with increasing k_z, as shown in Fig. 5(c). This is consistent with the observations in DNS. In addition, through comparison, it can be observed that the streamwise wavenumber spectrum and frequency spectrum predicted by WRLES are in excellent agreement with DNS results at low wavenumbers or low frequencies, but slightly lower at high wavenumbers and high frequencies. For the spanwise wavenumber spectrum, the agreement with DNS is also good in the low wavenumber range, but slightly overpredicted in the high wavenumber range. However, for WMLES, the spectrum is overpredicted in low wavenumbers or low frequencies ranges and underpredicted in high wavenumbers or high frequencies ranges. Meanwhile, in the streamwise wavenumber spectrum, WMLES predicts energy peak that is more

biased towards the high wavenumber region, consistent with the observations made by Park and Moin (2016).

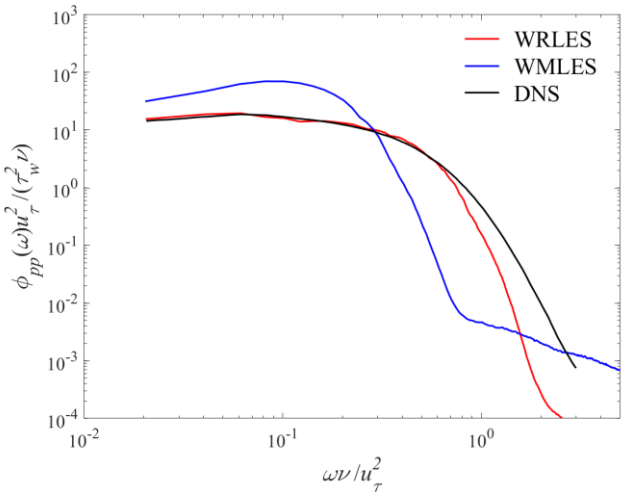

(a) Frequency

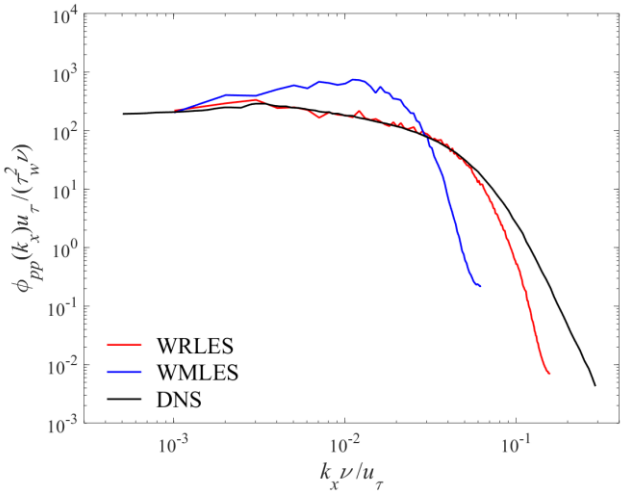

(b) Streamwise-wavenumber

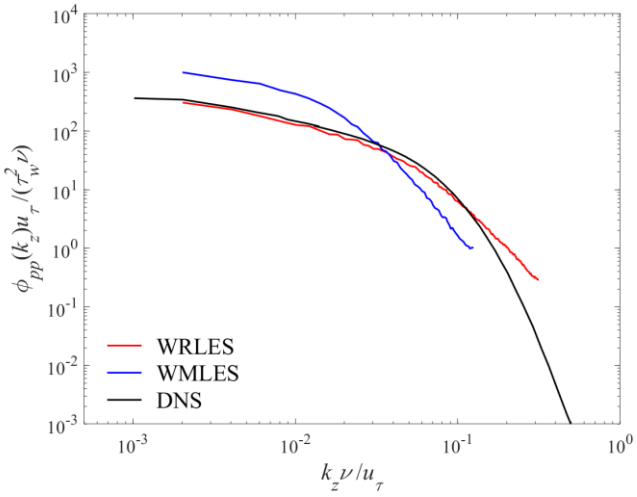

(c) Spanwise-wavenumber

Fig. 5 One-dimensional spectra of wall pressure fluctuations

Fig. 6 shows the two-dimensional wavenumber-frequency spectra obtained from WRLES and WMLES calculations. The two-dimensional spectral data are non-dimensionalized by δ, u_τ and τ_w. The plots display 5 contours of $\log_{10}\left[\phi_{pp}(k_x,\omega)\right]u_\tau/\delta^2\tau_w^2$ ranging from -7 to -3. Since the wavenumber-frequency spectrum is symmetric about the center $(k_x, \omega) = (0, 0)$, we only show the part where $k_x \geq 0$. The main purpose of studying wavenumber-frequency spectrum of turbulent wall pressure fluctuations is to understand the spatiotemporal correlation characteristics of turbulent structures and provide input for the vibration flow-generated structures and acoustic radiation of flow-generated noise, which is crucial for the development of predictive models for flow-generated noise.

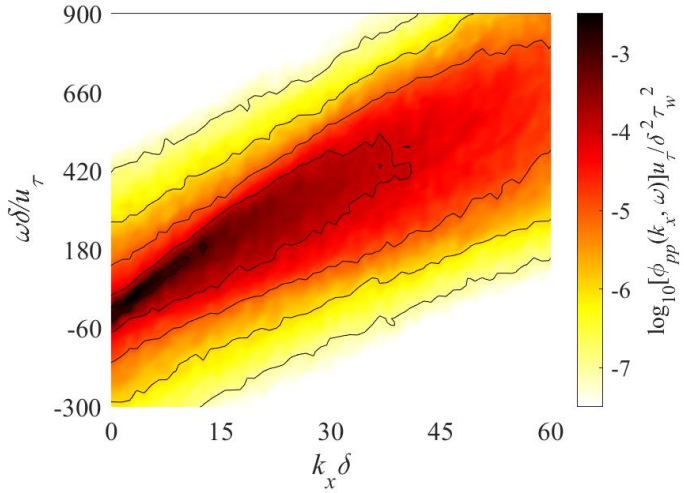

(a) WRLES

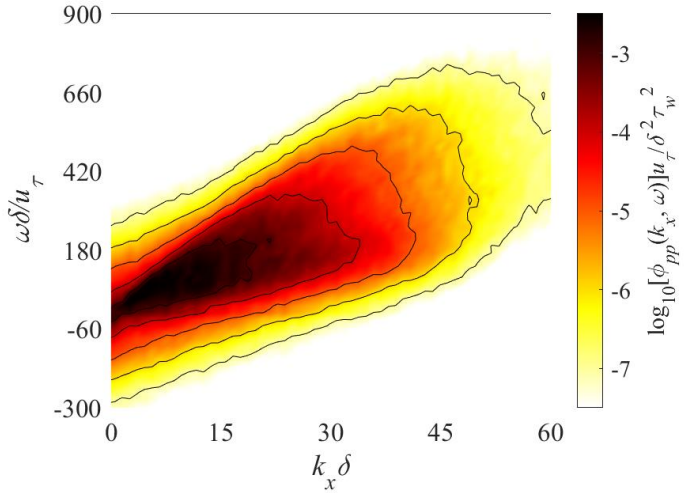

(b) WMLES

Fig. 6 Wavenumber-frequency spectra of wall pressure fluctuations

From the two-dimensional spectra, it can be observed that the spectral energy of wall pressure fluctuations at any frequency is concentrated near the convective wavenumber $k_c = \omega/u_c$, where u_c is the convective velocity, approximately 60%~80% of the bulk velocity U_b. The region where the spectral power is concentrated is called the "convective ridge". The slope of the convective ridge reflects the average convective velocity of quasi-ordered structures in turbulence. Its significance lies in the fact that when turbulent structures pass through an object at a speed equal to the convective velocity, their spatial morphology remains

unchanged. In addition, the width of the convective ridge increases with increasing frequency and wavenumber. The highest spectral level (the most energy-containing eddies) is distributed in the low-frequency and low-wavenumber range, and the energy decreases continuously with increasing frequency and wavenumber. This is in good agreement with experimental results (Abraham and Keith, 1998), DNS (Choi and Moin, 1990; Yang and Yang, 2022), and semiempirical models (Corcos, 1964; Chase, 1980), indicating that both WRLES and WMLES methods effectively capture the spatiotemporal correlation characteristics of near-wall turbulent fluctuating pressure. Another noteworthy point is that when the wavenumber k_x approaches zero, the contours gradually contract towards $(k_x, \omega) = (0, 0)$, especially at most energy-containing scales ($\log_{10}\left[\phi_{pp}(k_x,\omega)\right] u_\tau/\delta^2\tau_w^2$ = -3 and -4). This contraction behavior indicates that as k_x increases from zero, the spectrum of wall pressure fluctuations first increases and then decreases within a small range, consistent with the characteristics observed in the one-dimensional spectra shown in Fig. 5 (a) and (b). Additionally, compared to WRLES, the overall spectral level of WMLES results is significantly higher in the range of $k_x\delta < 30$ and $\omega\delta/u_\tau < 200$, leading to an overprediction in the integrated one-dimensional spectrum in the low-frequency and low-wavenumber regions. Moreover, the energy distribution range of WMLES spectra is more concentrated in the low-frequency and low-wavenumber regions compared to WRLES, resulting in a rapid decay of energy and difficulty in capturing the inertial subrange effectively. The main reason may be the relatively coarse near-wall grid of WMLES, especially in the streamwise and spanwise directions. Considering that the current wall model only models the near-wall velocity distribution and does not model the pressure distribution, this inevitably leads to prediction errors in wall pressure fluctuation.

Flow fields analysis

Fig. 7 shows the instantaneous vortical structures of the fully-development turbulent obtained from WRLES and WMLES, using the iso-surface of $\widetilde{\Omega}_R$ = 0.52 (Liu et al., 2018; Zhao et al., 2020) by the contour of Omega-Liutex. The visualization is colored by the dimensionless instantaneous streamwise velocity. Through the comparison, it can be observed that WRLES captures the structure of near-wall vortices more finely than WMLES. This further explains the observation in Fig. 5, where the high wavenumber spectral level predicted by WRLES is significantly higher than that of WMLES.

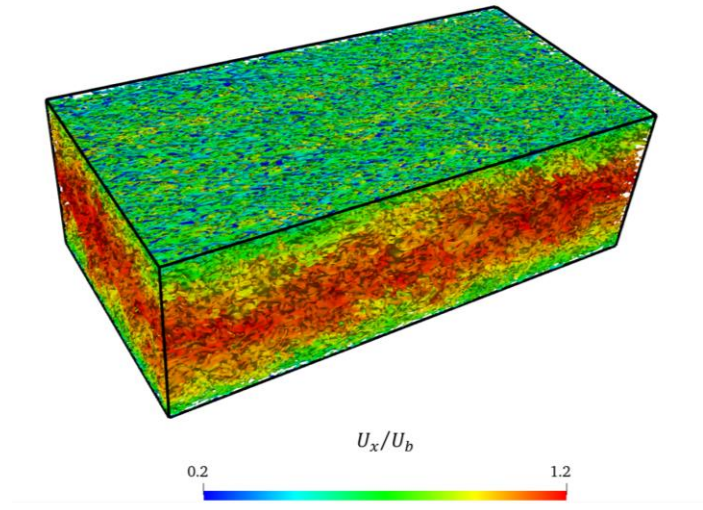

(a) WRLES

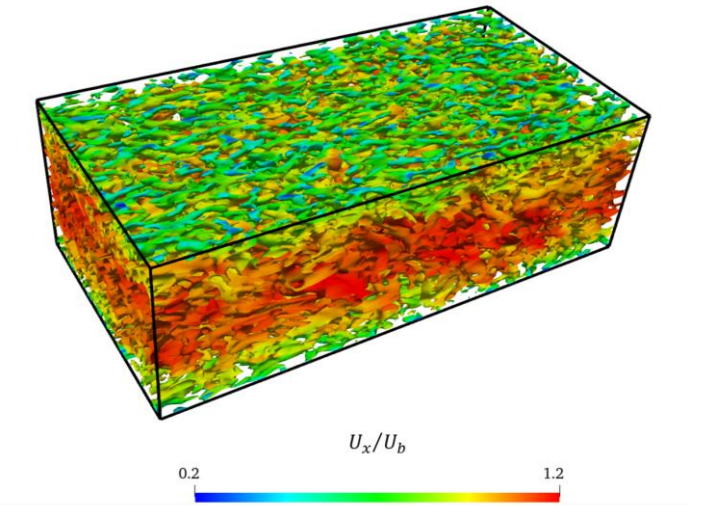

(b) WMLES

Fig. 7 Vortical structures of the fully developed channel flow

CONCLUSIONS

In this study, in order to evaluate the predictive accuracy of WMLES for wall pressure fluctuation, turbulent channel flow at $Re_\tau \approx 1000$ is numerically simulated using both WRLES and WMLES methods. In addition to comparing the near-wall velocity distribution and Reynolds stresses, we place special emphasis on the predictive accuracy of wall pressure fluctuation. The one-dimensional spectra and two-dimensional wavenumber-frequency spectra of wall pressure fluctuation are analyzed and compared with DNS data. The vortical structures of the fully developed channel flow are demonstrated. The main conclusions drawn from this study are as follows:

In terms of predicting time-averaged quantities, both WRLES and WMLES accurately predict the near-wall velocity distribution. The wall modeling effectively alleviates the LLM issue. In predicting Reynolds stresses, the results of WRLES are generally consistent with DNS, and WMLES aligns well with DNS in the outer layer of the boundary layer. However, in the modeled inner layer, the $\langle uu\rangle^+$ component is overpredicted, while the $\langle vv\rangle^+$ component is underpredicted.

In the prediction of wall pressure fluctuation, the one-dimensional spectral results of WRLES overall match well with DNS data, while WMLES exhibits a phenomenon of overestimating low-frequency (wavenumber) spectral levels and underestimating high-frequency (wavenumber) spectral levels. In terms of two-dimensional wavenumber-frequency spectra, both methods effectively capture the convective ridge where energy is concentrated. However, compared to WRLES, the energy distribution range of WMLES spectra is more concentrated in the low-frequency and low-wavenumber regions, with a rapid decay at high frequency (wavenumber). In conclusion, the current wall model only models the near-wall velocity distribution and does not model the pressure distribution, this inevitably leads to prediction errors in wall pressure fluctuation.

ACKNOWLEDGEMENTS

This work is supported by the National Natural Science Foundation of China (52131102), to which the authors are most grateful.

REFERENCES

Abraham, BM, and Keith, WL (1998). "Direct Measurements of Turbulent Boundary Layer Wall Pressure Wavenumber-Frequency Spectra," *J Fluids Eng*, 120(1), 29–39.

Chase, DM (1980). "Modeling the wavevector-frequency spectrum of turbulent boundary layer wall pressure," *J Sound Vib*, 70(1), 29–67.

Chen, S, Yang, L, Zhao, W, and Wan, D (2023). "Wall-modeled large eddy simulation for the flows around an axisymmetric body of revolution," *J Hydrodyn*, 35(2), 199–209.

Choi, H, and Moin, P (1990). "On the space-time characteristics of wall-pressure fluctuations," *Phys Fluids*, 2(8), 1450–1460.

Choi, H, and Moin, P (2012). "Grid-point requirements for large eddy simulation: Chapman's estimates revisited," *Phys Fluids*, 24(1), 011702.

Corcos, GM (1964). "The structure of the turbulent pressure field in boundary-layer flows," *J Fluid Mech*, 18(3), 353–378.

Fan, G, Liu, Y, Zhao, W, and Wan, D (2024). "Effect of wall stress models and subgrid-scale models for flow past a cylinder at Reynolds number 3900," *Phys Fluids*, 36(1), 015152.

He, K, Zhou, F, Zhao, W, Wang, J, and Wan, D (2024). "Numerical analysis of turbulent fluctuations around an axisymmetric body of revolution based on wall-modeled large eddy simulations," *J Hydrodyn*,.

Issa, RI (1986). "Solution of the implicitly discretised fluid flow equations by operator-splitting," *J Comput Phys*, 62(1), 40–65.

Jasak, H (1996). "Error analysis and estimation for the finite volume method with applications to fluid flows.,"

Larsson, J, Kawai, S, Bodart, J, and Bermejo-Moreno, I (2016). "Large eddy simulation with modeled wall-stress: recent progress and future directions," *Mech Eng Rev*, 3(1), 15–00418.

Liu, C, Gao, Y, Tian, S, and Dong, X (2018). "Rortex—A new vortex vector definition and vorticity tensor and vector decompositions," *Phys Fluids*, 30(3), 035103.

Martínez, J, Piscaglia, F, Montorfano, A, Onorati, A, and Aithal, SM (2015). "Influence of spatial discretization schemes on accuracy of explicit LES: Canonical problems to engine-like geometries," *Comput Fluids*, 117, 62–78.

Mukha, T, Rezaeiravesh, S, and Liefvendahl, M (2019). "A library for wall-modelled large-eddy simulation based on OpenFOAM technology," *Comput Phys Commun*, 239, 204–224.

Nicoud, F, and Ducros, F (1999). "Subgrid-scale stress modelling based on the square of the velocity gradient tensor," *Flow, Turbul Combust*, 62(3), 183–200.

Park, GI, and Moin, P (2016). "Space-time characteristics of wall-pressure and wall shear-stress fluctuations in wall-modeled large eddy simulation," *Phys Rev Fluids*, 1(2), 024404.

Piomelli, U, and Balaras, E (2002). "Wall-layer models for large-eddy simulations," *Annu Rev Fluid Mech*, 34(1), 349–374.

Sagaut, P (2005). "Large eddy simulation for incompressible flows: an introduction," *Springer Science & Business Media*.

Suga, K, Sakamoto, T, and Kuwata, Y (2019). "Algebraic non-equilibrium wall-stress modeling for large eddy simulation based on analytical integration of the thin boundary-layer equation," *Phys Fluids*, 31(7), 075109.

Van Driest, ER (1956). "On turbulent flow near a wall," *J Aeronaut Sci*, 23(11), 1007–1011.

Wang, M, and Moin, P (2002). "Dynamic wall modeling for large-eddy simulation of complex turbulent flows," *Phys Fluids*, 14(7), 2043–2051.

Wang, L, Hu, R, and Zheng, X (2020). "A comparative study on the large-scale-resolving capability of wall-modeled large-eddy simulation," *Phys Fluids*, 32(3), 035102.

Weller, H (2012). "Controlling the computational modes of the arbitrarily structured C grid," *Mon Weather Rev*, 140(10), 3220–3234.

Yang, B, and Yang, Z (2022). "On the wavenumber–frequency spectrum of the wall pressure fluctuations in turbulent channel flow," *J Fluid Mech*, 937, A39.

Yang, XIA, Park, GI, and Moin, P (2017). "Log-layer mismatch and modeling of the fluctuating wall stress in wall-modeled large-eddy simulations," *Phys Rev Fluids*, 2(10), 104601.

Zhao, W, Wang, J, and Wan, D (2020). "Vortex identification methods in marine hydrodynamics," *J Hydrodyn*, 32(2), 286–295.

Zhao, W, Zhou, F, Fan, G, and Wan, D (2023). "Assessment of subgrid-scale models in wall-modeled large-eddy simulations of turbulent channel flows," *J Hydrodyn*, 35(3), 407–416.